



**An all-in-one nanoparticle (AION) contrast agent for breast cancer screening with DEM-CT-MRI-NIRF imaging**

Journal:	<i>Nanoscale</i>
Manuscript ID	NR-ART-05-2018-003741.R1
Article Type:	Paper
Date Submitted by the Author:	22-Aug-2018
Complete List of Authors:	Hsu, Jessica; University of Pennsylvania, Bioengineering Naha, Pratap; University of Pennsylvania, Radiology Lau, Kristen; University of Pennsylvania, Radiology Chhour, Peter; University of Pennsylvania, Bioengineering Hastings, Renee; University of Pennsylvania, Radiology Moon, Brianna; University of Pennsylvania, Bioengineering Stein, Joel; University of Pennsylvania, Radiology Witschey, Walter; University of Pennsylvania, Radiology Mcdonald, Elizabeth; University of Pennsylvania Maidment, Andrew; University of Pennsylvania Cormode, David; University of Pennsylvania, Radiology

## **An all-in-one nanoparticle (AION) contrast agent for breast cancer screening with DEM-CT-MRI-NIRF imaging**

Jessica C. Hsu,<sup>1,2</sup> Pratap C. Naha,<sup>1</sup> Kristen C. Lau,<sup>1,2</sup> Peter Chhour,<sup>1,2</sup> Renee Hastings,<sup>1</sup> Brianna F. Moon,<sup>1,2</sup> Joel M. Stein,<sup>1</sup> Walter R. Witschey,<sup>1</sup> Elizabeth S. McDonald,<sup>1</sup> Andrew D. A. Maidment,<sup>1</sup> and David P. Cormode<sup>1,2,3\*</sup>

<sup>1</sup>Department of Radiology, University of Pennsylvania 3400 Spruce St, 1 Silverstein, Philadelphia, PA 19104, USA.

<sup>2</sup>Department of Bioengineering, University of Pennsylvania, Philadelphia, PA, USA.

<sup>3</sup>Department of Cardiology, University of Pennsylvania, Philadelphia, PA, USA.

\*Corresponding author

E-mail: david.cormode@uphs.upenn.edu; Tel: 215-615-4656; Fax: 215-662-7868

## Abstract

Conventional X-ray mammography has low diagnostic sensitivity for women with dense breasts. As a result, alternative contrast-enhanced screening tools such as dual energy mammography (DEM), computed tomography (CT), magnetic resonance imaging (MRI), and near-infrared fluorescence (NIRF) imaging are being used or investigated for these women. However, currently available contrast agents are non-ideal, have safety issues, and each imaging technique requires a different contrast agent. We therefore sought to develop a multimodal contrast agent that is functional for each breast imaging modality to simplify the diagnosis process and address the issues of existing contrast agents. Herein, we present a novel “all-in-one” nanoparticle (AION) multimodal imaging probe that has potent DEM, CT, MRI, and NIRF contrast properties and improved biocompatibility. AION were formed by co-encapsulation of a near-infrared fluorophore (DiR), silver sulfide nanoparticles ( $\text{Ag}_2\text{S-NP}$ ), and iron oxide nanoparticles (IO-NP) in PEGylated micelles. AION showed negligible cytotoxicity, which was in agreement with its minimal silver ion release profiles. AION generated strong contrast with all imaging modalities as demonstrated in phantom imaging. AION allowed *in vivo* tumor imaging as evidenced by the increase in contrast after injection. This study indicates the potential of AION as an effective multimodal contrast agent for breast cancer diagnosis with a range of imaging methods.

Keywords: silver sulfide, dual energy mammography, near-infrared, computed tomography, magnetic resonance, breast cancer

## Main text

The key to good prognosis of breast cancer is early detection. Currently, X-ray mammography is the gold standard for breast cancer screening and has been shown to reduce mortality from breast cancer.<sup>1</sup> Nevertheless, it is well established that diagnostic sensitivity of mammography is greatly reduced in women with dense breasts, who are about 50% of the screening population.<sup>2</sup> The sensitivity decreases from a level of 87% in women with less dense breasts to only 30-62% in women with dense breasts.<sup>3-4</sup> When mammography is used alone as a screening tool, decreased sensitivity may lead to delayed diagnosis, more advanced stage and reduced survival. Moreover, women with dense breasts have a three-fold higher risk of developing breast cancer, independent of issues related to screening.<sup>5</sup> Therefore, alternative screening tools are being developed for this population.

Contrast-enhanced imaging techniques such as magnetic resonance imaging (MRI), dual-energy mammography (DEM), computed tomography (CT), and near-infrared fluorescence (NIRF) imaging have emerged to improve breast cancer detection for women with dense breasts. These imaging modalities each use contrast agents to highlight breast abnormalities and overcome the masking effect from increased breast density. Screening breast MRI requires gadolinium-based contrast agents; however, free gadolinium ions can cause nephrotoxicity in patients with renal disease<sup>6-7</sup> and gadolinium deposits in the brain, with unknown effects.<sup>8-11</sup> Similarly, contrast-mediated nephropathy as well as patient allergic reactions are risks posed by iodinated contrast agents, such as iopamidol, which are commonly used in CT and DEM.<sup>12-14</sup> Moreover, iodinated agents produce suboptimal contrast especially in the case of DEM.<sup>15</sup> Improved contrast agents are needed for tumor detection and characterization with these imaging modalities.

Nanoparticles have potential as safe and effective contrast agents for numerous breast imaging modalities.<sup>15-21</sup> For example, iron oxide nanoparticles (IO-NP) provide contrast in T<sub>2</sub>- or

$T_2^*$ -weighted MRI that can be used for distinguishing lesions from normal tissues.<sup>22</sup> Silver nanoparticles have recently been identified to produce stronger contrast than iodinated agents in DEM.<sup>15, 21</sup> In addition, silver nanoparticles should provide CT contrast that is comparable to iodine as silver's k-edge at 25.5 keV allows for strong attenuation of lower energy X-rays.<sup>20</sup> However, to form stable and safe silver-based nanoparticles, a high percentage of gold inclusion was required,<sup>20</sup> resulting in a significant material cost. To overcome this cost issue, we herein propose silver sulfide nanoparticles ( $Ag_2S$ -NP) whose ultralow solubility constant ( $K_{sp} = 6.3 \times 10^{-50}$ ),<sup>23</sup> we hypothesized, would limit the release of silver ions, providing good biocompatibility, but with low material costs (the cost of sulfur is about \$0.09/kg).<sup>24</sup> Combining  $Ag_2S$ -NP, IO-NP and a NIRF fluorophore creates a multimodality agent for multiple imaging techniques. This will allow a safe and flexible screening option for intermediate and high risk patients, including women with dense breasts who need additional screening for improved sensitivity over conventional mammography. To our knowledge, the development of a multimodal contrast agent specific for breast cancer screening has rarely been explored. The integration of  $Ag_2S$ -NP, IO-NP and NIRF fluorophores into one platform has not previously been reported and provides functionalities for four different breast imaging modalities. This probe is uniquely designed to address issues related to current contrast agents. Moreover, the use of  $Ag_2S$ -NP as contrast agents for X-ray imaging has not previously been reported and there is only a handful of examples of novel contrast materials developed specifically for mammography.

In this study, we report a novel "all-in-one" nanoparticle (AION) multimodal contrast agent designed for noninvasive breast cancer detection using DEM, CT, MRI, and NIRF imaging modalities. AION were synthesized by encapsulating hydrophobic  $Ag_2S$ -NP, IO-NP, and DiR in mixed micelles formed with polyethylene glycol (PEG) modified phospholipids (Fig. 1A) *via* a one-pot ultrasonic emulsification procedure. The straightforward design of AION and their facile synthesis would be advantageous for clinical translation. Next, AION were characterized using various analytical tools such as transmission electron microscopy (TEM),

dynamic light scattering (DLS), scanning electron microscopy (SEM) and energy dispersive X-ray spectroscopy (EDX). After characterization, AION were investigated for their contrast generating potential with phantom imaging. *In vitro* cytotoxicity effects and silver ion leaching from AION were assessed. Lastly, *in vivo* imaging and biodistribution studies were performed in a murine model of breast cancer to evaluate the utility of AION as a multimodal contrast agent for breast cancer detection.

## Results and discussion

### Synthesis and characterization of AION

To synthesize AION, hydrophobic Ag<sub>2</sub>S-NP were first synthesized *via* a thermal decomposition single-source precursor approach adapted from previous reports.<sup>25-26</sup> This reaction resulted in dodecanethiol-coated Ag<sub>2</sub>S-NP with an average core diameter of  $4.7 \pm 1.2$  nm (Fig. 1B). The as-prepared Ag<sub>2</sub>S-NP, along with oleic-acid coated 10 nm IO-NP (Fig. 1C) and the lipophilic DiR fluorophore were encapsulated in the hydrophobic core of micelles composed of DSPC and DSPE-mPEG<sub>2000</sub> phospholipids (1:1 molar ratio) using a one-pot ultrasonic emulsification method. The 200:50:20:1 mass ratio of Ag<sub>2</sub>S-NP/phospholipids/IO-NP/DiR was chosen to prepare AION with a high payload of Ag<sub>2</sub>S-NP in order to achieve desirable DEM and CT contrast enhancement, while maintaining appropriate concentrations of IO-NP and DiR for sufficient MRI and NIRF contrast, respectively. Of note, PEGylated phospholipids were included as the carrier material due to their high stability and biocompatibility, as well as to deter opsonization and thus facilitate accumulation within the tumor *via* the enhanced permeability and retention (EPR) effect.<sup>27-29</sup> As a result, we did not observe significant changes in particle diameter (<5%) as determined by DLS when incubated in PBS containing 10% fetal bovine serum at 37 °C for 24 hours, proving its robust stability in physiological conditions.

The average core size and hydrodynamic diameter of AION were  $88 \pm 22$  nm and  $114 \pm 2.7$  nm as determined by TEM (Fig. 1D and E) and DLS, respectively. A polydispersity index of 0.161 was measured by DLS. The zeta potential of AION was found to be  $-42.5 \pm 0.8$  mV, indicating good stability towards coagulation or flocculation. The morphology of AION is indicated by SEM (Fig. S1). The EDX spectrum (Fig. S2) showed that AION have the expected 2:1 Ag:S stoichiometry and contain more silver than iron, which is consistent with the mass ratio used in the synthesis. A representative EDX line scan across a single AION particle is provided

in Fig. S3, which confirms the inclusion of both iron and silver within the same nanoparticle. AION have a broad UV-visible absorption band that is typical of  $\text{Ag}_2\text{S}$ -NP with an absorption peak at 748 nm, which corresponds to the excitation wavelength of DiR (Fig. S4).<sup>26</sup> Under excitation at 748 nm, a sharp fluorescence emission peak at 780 nm was observed that is again typical of DiR (Fig. S4). Both absorption and emission peaks of AION lie within the NIR region (650-900 nm), where tissue is more transparent to light.<sup>30</sup>

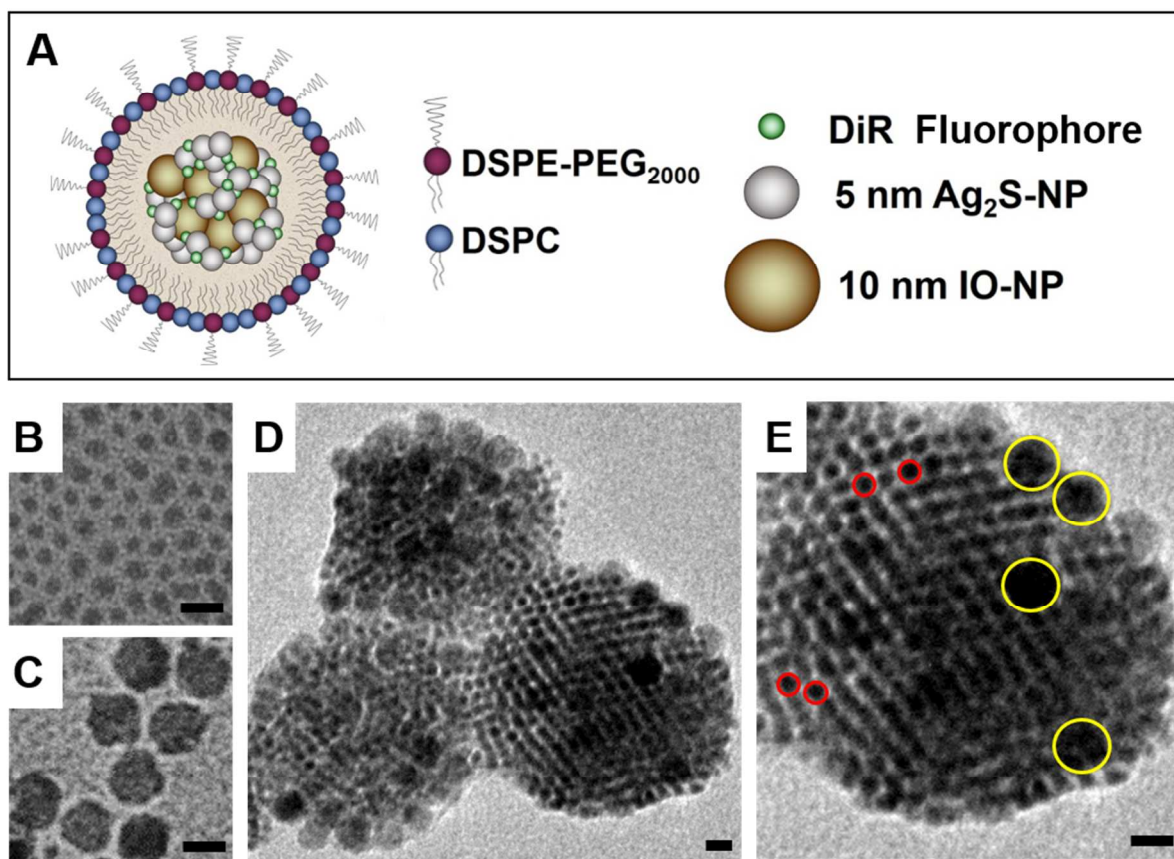


Figure 1. (A) Schematic depiction of AION structure and composition. TEM images of (B) as-prepared 4.7 nm  $\text{Ag}_2\text{S}$ -NP, (C) oleic acid coated 10 nm IO-NP, (D) AION particles and (E) an individual AION particle at a higher magnification showing the inclusion of  $\text{Ag}_2\text{S}$ -NP (red circles) and IO-NP (yellow circles). All scale bars are 10 nm.

### Silver ion leaching and *in vitro* cell viability

Although silver nanoparticles have been widely used in many consumer products, release of silver ions from these nanoparticles could pose a safety risk. We therefore evaluated the silver ion leaching potential of AION and a control silver nanoparticle (AgNP) by incubating them in two different media (DI water and citrate buffer at pH 5.5) at 37°C. AgNP were synthesized using a protocol consistent with AION preparation except for the incorporation of DT-coated elemental silver nanoparticles (5 nm in core diameter) instead of Ag<sub>2</sub>S-NP.<sup>31</sup> A TEM image of AgNP is shown in Fig. S5. Citrate buffer with a slightly acidic pH was used to simulate lysosomal fluid and the tumor microenvironment for the following reasons: 1) most silver nanoparticles are found in lysosomes after phagocytosis and 2) greater release of silver ions occurs at lower pH.<sup>32-34</sup> The results showed both AION and AgNP have similar silver ion release profiles with minimal release (~ 0.1%) over 7 days per the case of DI water (Fig. 2A). No statistical significance was found between the release profiles. However, as seen from Fig. 2B, a substantial amount of silver ions was released from AgNP (~ 0.4%) compared to AION (~ 0.1%) under slightly acidic conditions. Notably, no statistical difference was found between the release profiles of AION in neutral and acidic conditions, indicating the robust stability of these nanoparticles. These results are consistent with other reports in that elemental silver-based nanoparticles leach more silver ions at lower pH, and the ultralow solubility of Ag<sub>2</sub>S-NP prevents the release of silver ions.<sup>32, 35</sup>

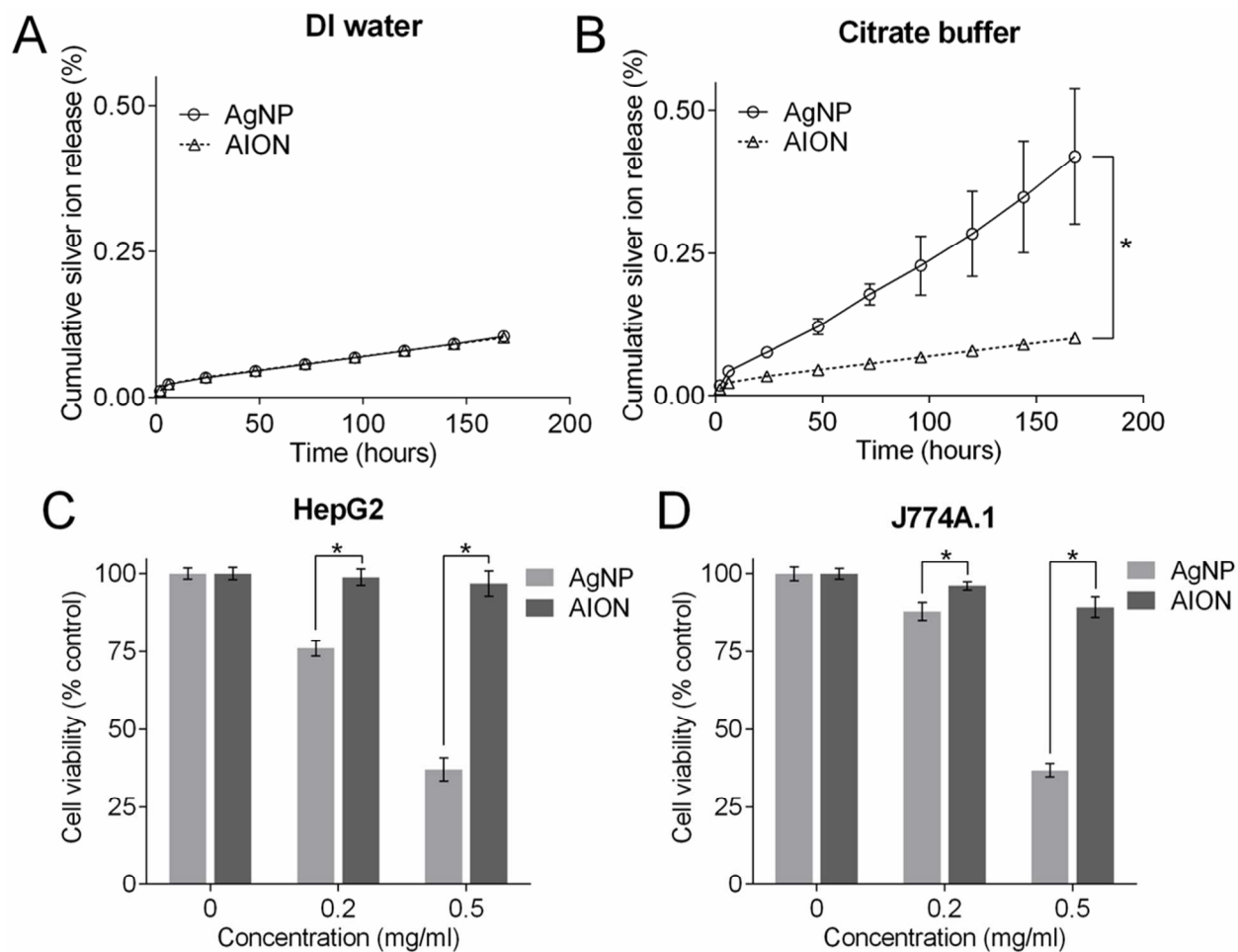


Figure 2. Silver ion release from AION and AgNP when incubated in (A) DI water and (B) citrate buffer (pH 5.5) at 37 °C over a period of 7 days. Viability of (C) HepG2 and (D) J774A.1 cells when incubated with AgNP and AION for 24 hours. Error bars are one standard deviation. Some error bars are hidden by the data point marker. \* indicates  $P < 0.05$  (unpaired Student's t-test).

To assess the effects of silver ion release, we examined the impact of AION on the viability of HepG2 and J774A.1 cells (Fig. 2C and D). These cells were incubated with AgNP and AION at two different concentrations (0.2 and 0.5 mg/ml of Ag) for 24 hours. The AION formulation was found to be biocompatible with both cell lines. However, when these cells were incubated with AgNP, their viability was significantly reduced compared to that of AION at each concentration. This result is in agreement with the observed silver ion release as more silver

ions were released from AgNP compared to AION. AgNP is a pure silver nanoparticle that is unstable towards oxidation and can release silver ions in biological conditions, which have previously been shown to cause cytotoxicity issues.<sup>36</sup> Overall, our hypothesis that use of Ag<sub>2</sub>S-NP would reduce silver ion release and improve biocompatibility of AION compared with pure silver nanoparticles was deemed correct.

### Phantom imaging

We performed phantom imaging to evaluate the contrast generating properties of AION with the various breast imaging modalities. The DEM contrast properties of AION (at a concentration of 17 mg Ag/ml) were investigated using a step phantom.<sup>37-38</sup> From Fig. 3A, it is evident that the background signal variations are removed and the contrast from AION is enhanced after DE subtraction. The signal difference-to-noise ratios (SDNR) calculated from the DE images indicate a significant increase in signal from background breast tissues when AION is present (Fig. 3B).<sup>15, 20</sup> Therefore, DEM imaging results indicated that AION is a suitable DEM contrast agent and that DEM subtraction can suppress the signal from the superimposing breast tissues and allow AION-containing breast tumors to be detected.

Since silver nanoparticles were previously shown to have CT attenuation properties, we expected similar results from AION.<sup>20, 39</sup> We evaluated the CT contrast properties of AION using a clinical CT imaging system. A CT phantom image of the different agents is presented in Fig. 3C. AION produce contrast that is linearly correlated with concentration, as is typical in CT (Fig. 3D).<sup>40</sup> Plots of CT attenuation versus concentration for all agents tested at each tube voltage are presented in Fig. S6. Examination of the CT attenuation rates revealed that AION attenuate X-rays slightly less than iopamidol and nearly identically to silver nitrate as expected (Fig. 3E). A statistical significance was found between the CT attenuation rates of AION and iopamidol at each tube voltage as expected. Additionally, CT attenuation rates given in units of HU/mM are presented in Fig. S7, where it can also be seen that AION produce slightly less contrast than

iopamidol. Notably, the CT attenuation rates of AION and iopamidol follow the same trend where the rates steadily decrease as the X-ray tube voltages increase from 80 to 140 kV. This is consistent with the fact that silver and iodine have k-edges (26 keV and 33 keV, respectively) that attenuate lower energy X-rays more strongly than higher energy X-rays. From these experiments, we conclude that AION produce CT contrast close to that of an iodinated agent and could serve as a CT contrast agent.

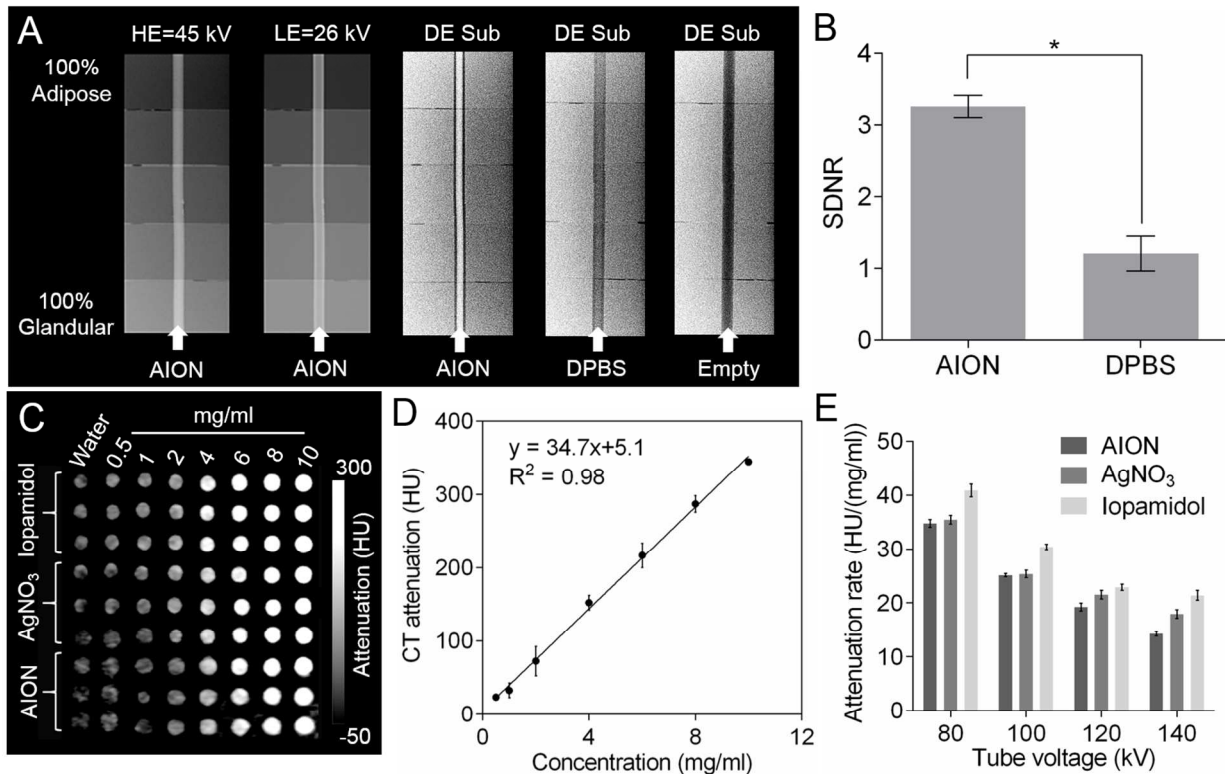


Figure 3. Phantom imaging of AION with X-ray based imaging modalities. (A) DEM phantom images (HE = high energy, LE = low energy, and DE Sub = dual energy subtraction) and (B) signal difference-to-noise ratios derived from (A). (C) CT phantom image and (D) CT attenuation of AION as a function of concentration at 80 kV. (E) CT attenuation rates of different agents for each tube voltage. Error bars are one standard deviation in all cases. \* indicates  $P < 0.05$  (unpaired Student's t-test).

An agar phantom containing different concentrations of AION was scanned with a clinical MRI scanner (Fig. 4A). It is evident that the signal is reduced with increasing concentrations of AION, as is expected from an iron oxide nanomaterial containing agent. The  $T_2$  values of these solutions decreased from 200 to 7.45 ms as AION concentrations increased from 0.01 to 0.32 mM. The transverse relaxivity ( $r_2$ ) was  $429.4 \text{ mM}^{-1}\text{s}^{-1}$  and the longitudinal relaxivity ( $r_1$ ) was  $8.3 \text{ mM}^{-1}\text{s}^{-1}$  resulting in a high relaxivity ratio ( $r_2/r_1$ ) of 51.7 at 3 T, demonstrating the potential of this agent for  $T_2$ -weighted MR imaging. Lastly, the NIRF contrast properties of AION were determined using an IVIS Spectrum imaging system and the default filter set for DiR (Fig. 4B). The fluorescence intensity observed becomes greater with increasing AION concentrations. Furthermore, we examined whether the metallic nanoparticles might have reduced the of the DiR fluorophore molecules. We first synthesized a control micellar DiR nanoparticle (mDiR) using a protocol consistent with AION preparation, but without the incorporation of  $\text{Ag}_2\text{S-NP}$  and  $\text{IO-NP}$ . We then compared the NIRF peak intensities of AION and mDiR at a fixed DiR concentration and found AION to in fact have higher NIRF signal. This indicates that the metallic nanoparticles within AION do not induce drastic quenching of the DiR fluorophores. In summary, phantom imaging studies have demonstrated that AION produce strong contrast *in vitro* and should be an effective contrast agent for *in vivo* breast tumor imaging.

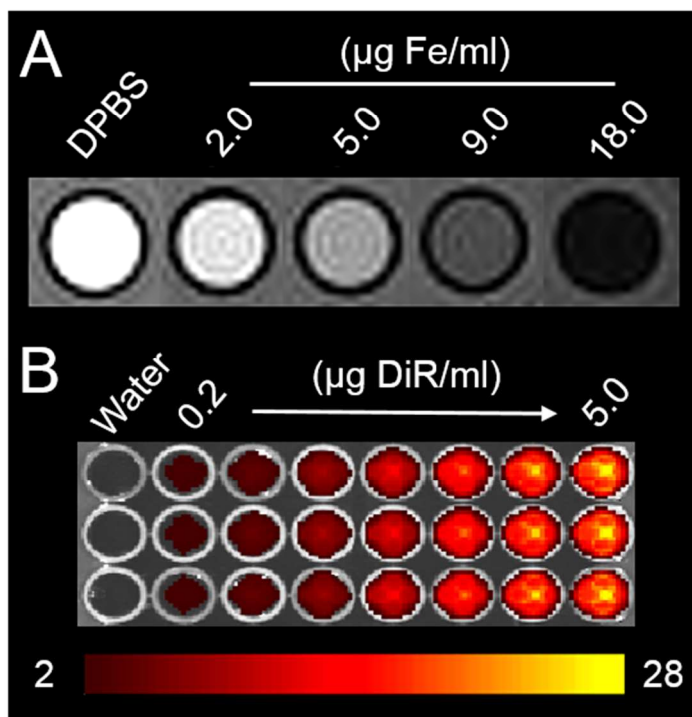


Figure 4. (A) MRI phantom image (the highest concentration corresponds to 90 µg Ag/ml) and (B) NIRF phantom image of AION (the highest concentration corresponds to 500 µg Ag/ml). Scale bar in units of radiant efficiency ( $\times 10^9$  (p/s/cm<sup>2</sup>/sr)/µW/cm<sup>2</sup>).

### ***In vivo* tumor imaging**

The promising results from *in vitro* biocompatibility analyses and phantom imaging encouraged us to investigate the applicability of AION as a safe and effective contrast agent for *in vivo* breast cancer imaging. The *in vivo* imaging experiments were performed using mice inoculated with human breast cancer cells. After pre-injection scans were done, the mice were injected with AION at a concentration of 250 mg Ag/kg (or 25 mg Fe/kg for MRI) and imaged with DEM, CT, MRI, and NIRF systems at various time points. Of note, shorter post-injection time points (*i.e.* 5-120 minutes) were chosen for DEM to align with the current clinical imaging procedure with this modality. The representative DEM images shown in Fig. 5A indicated that the DEM contrast at the tumor site (in red dashed circles) is increased when compared to the

pre-injection scan. The CNR in the tumors (Fig. 5B) was significantly higher after injections of AION, at all time points. No significant differences in signal were found among the post-injection time points imaged with DEM. Similar results were obtained from *in vivo* CT breast tumor imaging experiments as presented in Fig. 5C. Significantly higher CT attenuation and contrast were found in the tumors at both post-injection time points compared to the pre-injection scan (Fig. 5D). There is no significant difference in the CT attenuation between the two post-injection time points. These increases in tumor contrast post-injection are consistent with the *in vivo* DEM imaging results and indicate that AION have potential as contrast agents for breast cancer screening with CT, which could have use with future clinical breast CT scanners.<sup>41-42</sup>

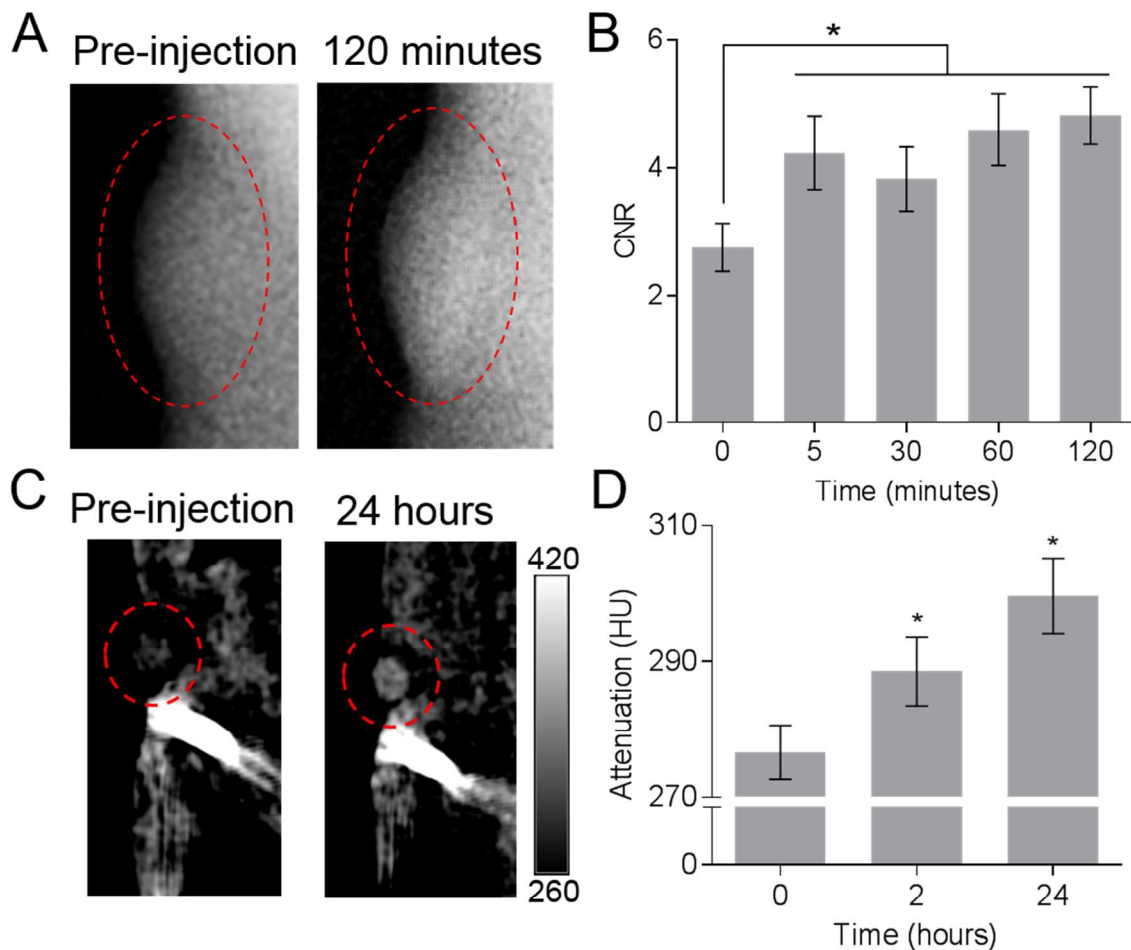


Figure 5. *In vivo* tumor imaging with AION using X-ray based imaging modalities. (A) DEM images of representative tumor-bearing mice at pre-injection and 120 minutes post-injection with AION. (B) DEM image-derived contrast-to-noise ratios in the tumor regions at the time points imaged. (C) CT images of a representative tumor-bearing mouse pre-injection and at 24 hours post-injection. Scale bar in units of CT attenuation (HU). (D) Average CT attenuation at pre-injection and 2 and 24 hours post-injection. Error bars are standard error of mean. Red dashed ovals indicate tumors. Pre-injection is noted as 0 hours for both graphs. \* indicates  $P < 0.05$  compared to pre-injection scans (paired Student's t-test).

For *in vivo* MR imaging, we scanned the tumor-bearing mice using a 4.7 T small animal MR system. Representative  $T_2$ -weighted MR images and the corresponding transverse relaxation rate ( $R_2$ ) maps at the level of tumor of a mouse before and after injection of AION are shown in Fig. 6A. The mean  $R_2$  values over the tumor ROI significantly increased from  $51 \pm 5$  Hz to  $75 \pm 17$  Hz with the injection of AION. Pixel-wise squared correlation coefficient was used to examine the quality of the curve fitting and a mean value of  $0.93 \pm 0.04$  was found across the tumor regions, indicating a reliable  $R_2$  measurement. Notably, the inherent heterogeneity of the tumor tissues causes localized deposition of AION within the tumors which led to large variations in tumor signal intensity as observed by MRI. Lastly, we evaluated the *in vivo* NIRF contrast properties of AION using the aforementioned fluorescence imaging system (Fig. 6B). The average NIRF tumor-to-background ratio (TBR) significantly increased after injections of AION (Fig. 6C). The TBRs at the 2 and 24 hour post-injection time points were not found to be significantly different. Overall, this result is in good agreement with the other contrast-enhanced imaging modalities as AION can readily improve breast tumor conspicuity *in vivo*.

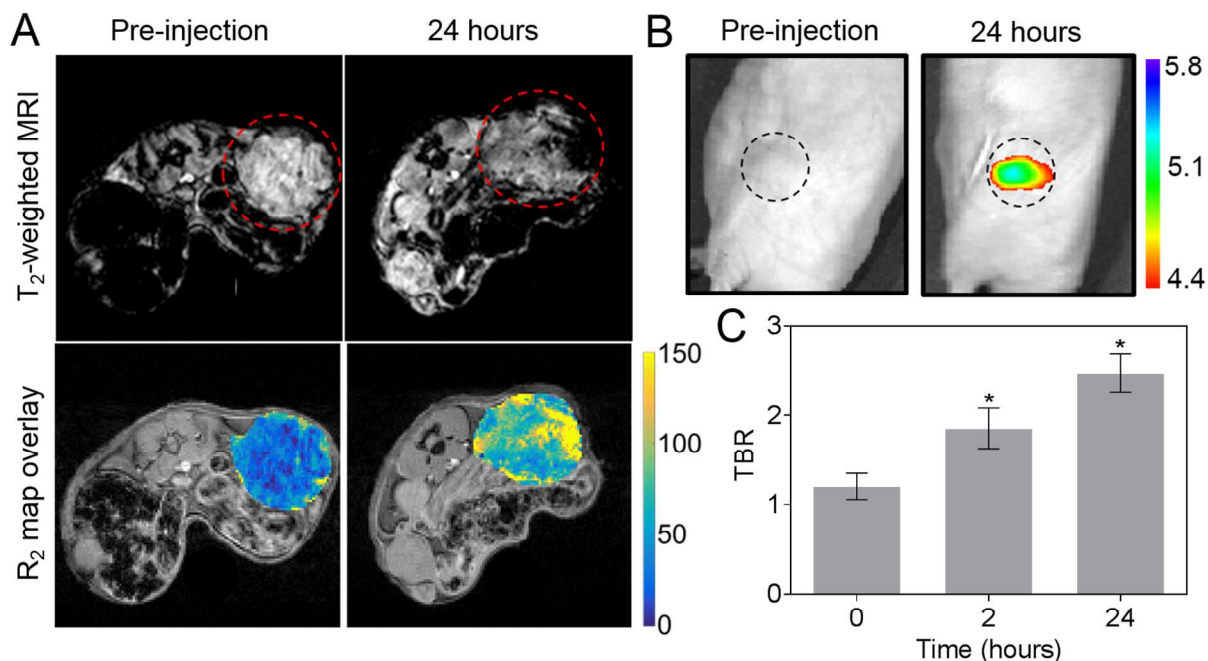


Figure 6. *In vivo* MRI and NIRF optical imaging with AION. (A) Top: MR images of representative tumor-bearing mice pre-injection and at 24 hours post-injection with AION. Images are shown with TE of 13.2 ms. Red dashed circles indicate tumors. Bottom: representative R<sub>2</sub> maps of the same mouse tumor before and after injection of AION. Scale bar in units of Hz (1/s). (B) NIRF images of representative tumor-bearing mice with AION at different time points. Black dashed circles indicate tumors. Scale bar in units of radiant efficiency ( $\times 10^9$  (p/s/cm<sup>2</sup>/sr)/μW/cm<sup>2</sup>). (C) Tumor-to-background ratio calculated from the NIRF images with AION. Error bars are standard error of mean. \* P < 0.05 compared to pre-injection scan (paired Student's t-test).

### Biodistribution and pathology analysis

At 24 hours post-injection, animals were sacrificed and their organs and tumor tissues were collected for biodistribution analysis. The silver content in the tissues was determined using ICP-OES as shown in Fig. 7. The results indicated that higher amounts of AION are taken up by the liver and spleen, which are the organs responsible for opsonization and

reticuloendothelial phagocytosis. This finding is not atypical as other studies have reported similar results with comparable nanoparticle designs.<sup>43-44</sup> Additionally, the animals did not show any adverse effects after injection with AION. Moreover, some degree of tumor accumulation is observed (more than 1% injected dose per gram of tissue), suggesting that the combination of surface PEGylation and particle size of AION facilitated their accumulation at the tumor site *via* the EPR effect. It is interesting to note that this level of tumor accumulation is sufficient to readily improve tumor conspicuity, at the dose used. Nevertheless, the design of AION could be modified to include higher molecular weight PEG ligands in order to provide more substantial stealth characteristics for evading the reticuloendothelial system (RES), thereby increasing the accumulation level of AION to further enhance contrast in tumors.<sup>45-46</sup>

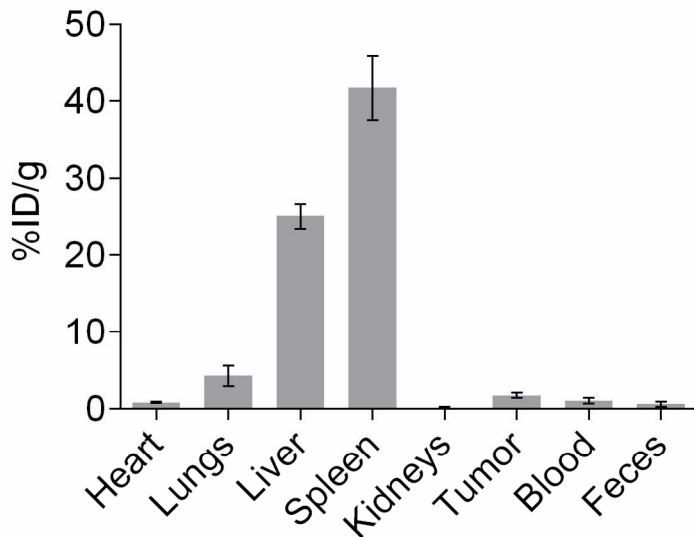


Figure 7. Biodistribution of AION (silver content analyzed by ICP-OES) in tumor tissues and major organs at 24 hours post-injection.

To assess the *in vivo* safety of AION, we performed histopathological examination of organs (i.e. liver and spleen). Necropsy was performed at 24 hours after injection of AION at a

dose of 250 mg Ag/kg and organs were fixed and stained with H&E for pathology analysis. As shown in Fig. S8, no evident histopathological abnormalities or lesions were observed from the treated mice in comparison with the control. These preliminary findings support the *in vivo* safety of the AION contrast agent.

The sensitivity of conventional mammography is poor in women with dense breasts, primarily due to the masking effect from superimposing fibroglandular tissues.<sup>2</sup> Women with high breast density also have an increased chance of developing breast cancer, which is an inherent risk apart from issues related to screening.<sup>5</sup> These women are a vulnerable population and often require alternative screening methods for more accurate diagnosis of breast cancer. Other imaging techniques such as contrast-enhanced DEM, CT, MRI, and NIRF imaging are being used or explored. These techniques are less affected by breast density and can highlight tumors *via* use of contrast agents. Several studies indicate that DEM and MRI have improved specificity and low false positive rates compared with conventional mammography, where the specificity is often limited, leading to unnecessary workups and benign biopsies. Furthermore, DEM has potentially better specificity than MRI due to linearity of contrast with agent concentration in X-ray imaging.<sup>47-49</sup>

Some of these techniques are already being used clinically; however, they can vary widely in terms of cost, availability, and patient comfort. For instance, MRI is expensive, is not readily available, and is not applicable to patients with claustrophobia or contraindications such as pacemakers and metal implants.<sup>50-52</sup> More recently, gadolinium based contrast agents for MRI were found to accumulate in neural tissues even in subjects with normal renal function and remain there for a long time.<sup>8-11</sup> The health effects from long-term retention of gadolinium in the brain are currently unknown. This finding provides incentive to develop alternative and improved contrast agents especially for women with elevated breast cancer risks as they commence screening in their 20s and continue for many years. Moreover, each of the imaging methods requires a different contrast agent, which can be problematic if supplemental screening is

needed. The administration of multiple doses of agents can pose a safety concern as additional stress is being put on the body's clearance mechanisms. Therefore, it is highly advantageous to create a single probe that avoids the use of gadolinium or iodine based contrast agents to ensure safety and is functional for a variety of breast imaging modalities to provide flexibility in the diagnosis process. With the integration of several imaging modality agents, this multimodal nanoprobe could combine information from each individual imaging modality to provide complementary data, enhancing diagnostic specificity.<sup>53</sup>

In this study, we developed AION as a multimodal contrast agent that improves tumor conspicuity with the aforementioned breast cancer imaging methods. AION are composed of two metal nanoparticles (*i.e.* IO-NP and Ag<sub>2</sub>S-NP) and a NIRF fluorophore (*i.e.* DiR). In particular, IO-NP generate T<sub>2</sub> contrast and are generally regarded to be safer and more biocompatible than gadolinium based nanoparticles due concern over the consequences of long-term gadolinium retention.<sup>54</sup> We chose Ag<sub>2</sub>S-NP as the material for DEM and CT contrast generation owing to their excellent biocompatibility that resulted from their very low solubility product. Ag<sub>2</sub>S-NP are also much lower in cost than gold-silver alloys (GSAN), a comparable DEM and CT agent. With the current metal prices (*i.e.* \$0.55/g and \$41.01/g for silver and gold, respectively),<sup>55-56</sup> the cost of a dose of 250 mg Ag/kg for a woman of average weight would be \$10 for AION versus \$330 for GSAN. The price would therefore be reduced by at least 30-fold with the use of silver sulfide-based agent (compared to GSAN with inclusion of 20% gold). Furthermore, Ag<sub>2</sub>S-NP were previously shown to emit in the second NIR window (950-1350 nm), which is more desirable than the first NIR window due to lower photon absorption/scattering and tissue autofluorescence.<sup>26, 57</sup> This allows for imaging of deeper tissues and organs with enhanced signal-to-noise ratio. Therefore, it is possible to exclude DiR from the formulation and instead use Ag<sub>2</sub>S-NP to provide NIRF signal when NIR-II imaging systems become more widely available.

AION were shown to release a minimal amount of silver ions when incubated in both neutral and slightly acidic conditions. Of note, this study was performed without the use of any media that contains chloride ions, especially physiological buffers such as PBS or PBS with 10% serum. This is because the released silver ions can react with the chloride ions in the media to form silver chloride precipitates that are difficult to separate from the silver nanoparticles and be collected in the filtrate. The results for silver ion release may therefore be rendered inaccurate in such experiments. Interestingly, the overall cumulative silver ion release (%) in both conditions is substantially (at least five-fold) lower than that of PEG-thiol-coated silver nanoparticles (*i.e.* 0.7% in DI water and 2.5% in citrate buffer over 7 days).<sup>20</sup> This could be explained by the lipid coating of the nanoparticles preventing access to the silver nanoparticle surfaces.<sup>27</sup> Thus, we attributed the minimal silver ion release of AION to both the phospholipid coating and the low solubility of Ag<sub>2</sub>S-NP.

Our study has limitations, there was some level of elemental silver (or AION) accumulation in the liver and spleen after injection. Although this finding is not atypical, the surface PEGylation and particle size could be modified to slow their clearance by the RES and further increase their accumulation at the tumor site. As mentioned earlier, the inclusion of higher molecular weight PEG (*e.g.* 5k) on the particle surface could better deter opsonization and evade the RES. Moreover, decreasing the nanoparticle size from 200 nm might also improve tumor accumulation.<sup>29</sup>

Notably, the contrast in the tumors was elevated over a range of time points. This could be beneficial for future clinical applications as AION can provide contrast for many hours after administration which eliminates the need for swift post-injection imaging as seen with current contrast agents, allowing for flexible scheduling and planning. Future directions for this platform might include the synthesis of ultra-small (< 5 nm) aqueous-phase silver based nanoparticles that can be swiftly excreted renally. This is advantageous as excretion from the body is an important criterion for FDA approval of a nanoparticle based contrast agent. Furthermore, these

particles can be encapsulated in biodegradable polymeric nanoparticles for increased circulation time and enhanced tumor accumulation.<sup>58</sup> Lastly, AION are a promising contrast agent for DEM and may have use in the emerging technique of photon-counting spectral mammography.<sup>59-60</sup>

## Conclusion

In this study, we developed an “all-in-one” multimodal nanoparticle contrast agent for use by multiple breast cancer imaging techniques. AION were synthesized by incorporating Ag<sub>2</sub>S-NP, IO-NP, and DiR in the hydrophobic core of phospholipid micelles. We included Ag<sub>2</sub>S-NP in the formulation to provide DEM contrast and minimize the release of silver ions that can cause safety concerns. This was confirmed by the *in vitro* silver ion leaching and cell viability studies where minimal silver ion release and negligible cytotoxicity were found. AION produced strong DEM, CT, MR, and NIRF contrast in phantoms and *in vivo*. Accumulation of AION in tumors allowed *in vivo* imaging at multiple times points after the administration of AION. Therefore, AION have potential as a safe and effective multimodal contrast agent for a range of breast cancer imaging techniques.

## Materials and methods

**Materials.** Silver diethyldithiocarbamate ((C<sub>2</sub>H<sub>5</sub>)<sub>2</sub>NCS<sub>2</sub>Ag, 99%), 1-dodecanethiol (DT, 98%), and silver nitrate (AgNO<sub>3</sub>, 99%) were purchased from Sigma-Aldrich (St. Louis, MO). Oleic-acid coated 10 nm IO-NP in chloroform and 1,1'-dioctadecyl-3,3,3',3'-tetramethylindotricarbocyanine iodide (DiR) powder were purchased from Ocean NanoTech (San Diego, CA) and Thermo Fisher Scientific (Eugene, OR), respectively. Both 1,2-distearoyl-*sn*-glycero-3-phosphocholine (DSPC) and 1,2-distearoyl-*sn*-glycero-3-phosphoethanolamine-N-[methoxy(polyethylene glycol)-2000] (DSPE-mPEG<sub>2000</sub>) were purchased from Avanti Polar Lipids (Alabaster, AL). All

chemicals were used without further modifications and Milli-Q deionized (DI) water (18.2 MΩ.cm) was used throughout the entire study.

**Synthesis of Ag<sub>2</sub>S-NP and AION.** Hydrophobic Ag<sub>2</sub>S-NP with an average core size of 4.7 nm were synthesized using methods based on previous reports.<sup>25-26</sup> In brief, 26 mg of (C<sub>2</sub>H<sub>5</sub>)<sub>2</sub>NCS<sub>2</sub>Ag was added to 10 g of DT in a 100 ml three-neck round-bottom flask at room temperature. The reaction mixture was placed under reduced pressure using house vacuum for 10 minutes with constant stirring. Then, N<sub>2</sub> was introduced to create an inert atmosphere for the reaction mixture, while being heated to 210 °C at a heating rate of 15 °C/min using a temperature controlled heating mantle. The reaction was kept at 210 °C for 1 hour. After the reaction was completed, the mixture was allowed to cool to room temperature. The product was precipitated *via* addition of 50 ml of absolute ethanol and isolated by centrifugation at 7000 rcf for 20 minutes. The supernatant was discarded and the pellet was resuspended in 50 ml of ethanol and isolated again by centrifugation using the same parameters. After repeating this process three times, the as-prepared DT-coated Ag<sub>2</sub>S-NP were dried for subsequent use in formation of AION.

A combined solution (1 ml) of Ag<sub>2</sub>S-NP (20 mg), IO-NP (2 mg), DiR (100 µg), DSPC (1.1 mg) and DSPE-mPEG<sub>2000</sub> (3.9 mg) suspended in chloroform and methanol was added to a glass vial containing 10 ml of DI water. The mixture was emulsified for approximately 10 seconds using a bath sonicator and was allowed to gently stir uncovered overnight in order to allow chloroform evaporation. The resulting solution was centrifuged at 2630 rcf for 10 minutes and was then filtered through a 0.22 µm filter (EMD Millipore, Billerica, MA) to remove aggregates. Using 10 kDa MWCO ultrafiltration tubes (Sartorius Stedim Biotech, Germany), the nanoparticles were concentrated and washed three times with DI water. Finally, all empty micelles and smaller sized particles were removed *via* potassium bromide (KBr) density gradient centrifugation. This was done by gently adding 200 µl of the concentrated AION sample on top

of the 1.3 g/ml KBr solution (1 ml) in a 1.5 ml Eppendorf tube. Then, the tubes were spun at 14,500 rpm for 1 hour. After centrifugation, 300  $\mu$ l at the top of the solution was carefully removed and discarded. 20 ml of DPBS was added to the remaining solution containing AION, then AION was washed thrice with DPBS and concentrated using 10kDa MWCO ultrafiltration tubes, and stored at 4°C for future use.

### **Characterization.**

*Transmission electron microscopy.* Both Ag<sub>2</sub>S-NP and AION samples were examined using an FEI Tecnai T12 electron microscope with an acceleration voltage of 120 kV. Formvar carbon-coated copper grids with 200 mesh (Electron Microscopy Sciences, Hatfield, PA) were used to prepare the TEM samples. Briefly, 10  $\mu$ l of diluted Ag<sub>2</sub>S-NP or AION samples (5  $\mu$ l from concentrated stock diluted with 495  $\mu$ l DI water) were dropped onto the grids and allowed to dry before imaging. The core diameter of AION was measured using ImageJ (National Institutes of Health, Bethesda, MD).

*Scanning electron microscopy and energy dispersive X-ray spectroscopy.* To prepare for analysis, AION samples were drop casted onto an aluminum substrate and dried completely in a vacuum. An FEI Quanta 600 FEG scanning electron microscope operated at 20 kV and equipped with EDX spectrometry (EDAX, Inc.) was used to acquire SEM images and EDX spectra and line scan measurements of AION.

*Dynamic light scattering and zeta potential.* The hydrodynamic diameter and zeta potential of AION were measured using a Nano ZS-90 Zetasizer (Malvern instrument, UK). In brief, 10  $\mu$ l of AION from the stock were diluted with 2 ml of DI water. 1.5 ml and 1 ml of nanoparticle suspension were used for the measurement of hydrodynamic diameter and zeta potential,

respectively. The number mean was reported for the hydrodynamic diameter. All measurements were performed at 25 °C.

*UV/visible absorption and fluorescence spectroscopy.* The UV/visible absorption spectrum of AION was measured by an UV/visible spectrophotometer (Thermo Fisher Scientific, USA). In brief, 100 µl from AION stock (DiR concentration: 4.4 µg/ml) were diluted with 2900 µl of DI water. The diluted samples were used to record UV-visible spectra and fluorescence spectrum. The absorbance spectrum was normalized to a maximum absorbance of 1. The NIR fluorescence spectrum was obtained using a SpectraMax M5 microplate reader (Molecular Devices, Sunnyvale, CA) with an excitation wavelength of 748 nm.

*Inductively coupled plasma optical emission spectroscopy.* The silver and iron concentrations of AION were determined using ICP-OES (Spectro Genesis ICP). The samples were prepared by dissolving 10 µl of AION stock solution in 1 ml of concentrated nitric acid and making the final volume to 10 ml with DI water.

**Silver ion leaching.** The silver ion release experiments were done as per a previously published procedure.<sup>20</sup> Briefly, 50 µl of AION (from 100 mg Ag per ml stock) were added to 4950 µl of DI water or simulated lysosomal fluid (citrate buffer at pH 5.5) and incubated at 37 °C. Samples were collected from the larger volume using 10 kDa MWCO ultrafiltration tubes at the following time intervals: 1, 2, 6, 24, 48, 72, 96, 120, 144, and 168 hours. Three independent experiments were done for each time point. The cumulative silver ion released (%) was calculated and presented as mean ± SD for each time point.

**Cell viability assay.** HepG2 (human hepatocellular liver carcinoma) and J774A.1 (murine macrophages) cell lines were purchased from ATCC (Manassas, VA) and cultured according to

the supplier's instructions. *In vitro* cytotoxicity of AION was evaluated using the LIVE/DEAD assay (Invitrogen Life Technologies, Grand Island, NY). In brief, 80,000 cells were seeded in 20 mm diameter glass bottom dishes with the appropriate cell culture media supplemented with 10% fetal bovine serum and 1% streptomycin/penicillin and incubated at 37 °C under 5% CO<sub>2</sub>. After 24 hours of incubation, cells were treated with AION or AgNP dispersed in cell culture media at either 0.2 or 0.5 mg Ag/ml. Once the treatment period of 24 hours was complete, the cells were washed once with sterile DPBS and incubated with 400 µl of LIVE/DEAD cocktail (2 ml DPBS, 0.5 µl stock calcein-AM, 1 µl stock ethidium-1 homodimer and 2 µl 3.2 mM Hoechst 33342) for 20 minutes. The cells were then imaged using Nikon Eclipse Ti-U fluorescence microscope with DAPI (ex: 359, em: 461 nm), FITC (ex: 495, em: 519 nm), and Texas Red (ex: 595, em: 613 nm) filters. Four images were taken per plate for each channel. The number of cells for the calcein-AM, ethidium-1 homodimer and Hoeschst stain for each sample was counted using a custom MATLAB (MathWorks, Natick, MA) program. The viability percentage was determined by taking the ratio of living cells to total number of cells. The relative cell viability (% control) is presented as mean ± SD for each concentration and cell line. Three independent experiments were performed.

### **Phantom imaging.**

*Dual energy mammography.* The DEM contrast properties of AION were investigated using a step phantom.<sup>15</sup> This step phantom was fabricated using materials that attenuate X-rays similarly to glandular and adipose tissues *i.e.* the major X-ray attenuating components of breast tissues. These background materials are arranged so that the composition of the phantom varies from 100% glandular to 100% adipose tissues. A Tygon plastic tube containing AION (17 mg Ag/ml) was inserted into a channel through the center of the longitudinal direction of the step phantom. Then, a Hologic Selenia Dimensions prototype DEM system (Bedford, MA) was used to image the phantom containing AION by acquiring two mammograms with two distinct X-ray

tube voltages and beam filters. The high energy (HE) images were acquired at 45 kV and 40 mAs, while the low energy (LE) images were acquired at 26 kV and 100 mAs. Copper and silver filters were used for the HE and LE X-rays, respectively. Finally, a logarithmically weighted subtraction between the LE and HE images was performed to create a dual energy (DE) image as described in previous studies.<sup>15, 20-21</sup> A total of three scans was performed. The mean DEM signal intensities generated from AION, DPBS and empty tube (background without contrast) were measured using ImageJ by placing a rectangular ROI on the target in each image. The SDNR (equation 1) was calculated and presented as mean  $\pm$  SD.

$$SDNR = \frac{|DEM\ signal\ (AION\ or\ DPBS) - DEM\ signal\ (background)|}{noise\ of\ background} \quad \text{Equation (1)}$$

*Computed tomography.* The CT phantom was constructed according to a previously reported method.<sup>40</sup> In brief, different concentrations (0.5 to 10 mg/ml, diluted with DI water) of iopamidol, AgNO<sub>3</sub>, and AION were placed into PCR tubes that were later secured in a plastic rack. Negative controls were prepared using DI water and PBS. The phantom included three replicates for each concentration and each agent. The rack was immersed in water (21 cm in height) and scanned with a Siemens SOMATOM Force clinical CT scanner at 80, 100, 120, and 140 kV. The images were acquired using the following parameters: tube current = 360 mA, matrix size = 512 x 512, slice thickness = 0.5 cm, field of view (FOV) = 37 x 37 cm. Osirix 64 bit was used to determine the attenuation values in Hounsfield units (HU) for each sample tube using the ROI analysis tool. CT attenuation rates (HU·ml/mg and HU/mM) were calculated for each agent at each voltage and presented as mean  $\pm$  SD.

*Magnetic resonance imaging.* The MRI phantom was prepared by placing AION samples of different concentrations (0.01 to 0.32 mM based on iron, diluted with DI water) in a 2% agar gel doped with 0.35 mM manganese chloride. The phantom was scanned using a Siemens

Magnetom Trio with a 3 T magnet.  $T_1$ -weighted spin-echo and inversion recovery pulse sequences were used to obtain  $T_1$  relaxation times and  $T_1$ -weighted MR images. The MR imaging parameters were: echo time (TE) = 5.8 ms, repetition time (TR) = 10000 ms, slice thickness = 3 mm, flip angle (FA) = 180 degrees, imaging matrix = 256 x 256, field of view (FOV) = 180 x 180 mm and number of averages (NA) = 2. Multiple inversion time (TI) values were chosen and shown as follows: 50, 100, 150, 200, 300, 400, 600, 700, 800, 900, 1000, 1400, 1800, 2200, 3000, 4000, 5000 and 6000 ms. The  $T_2$  relaxation times and  $T_2$ -weighted MR images were determined using a spin-echo sequence with the following parameters: TR = 10000 ms, slice thickness = 3 mm, NA = 1, FA = 90 degrees, imaging matrix = 256 x 256 and FOV = 180 x 180 mm. Multiple TE values were chosen and shown as follows: 6.6, 8.8, 11, 13, 15, 20, 25, 30 and 40 ms. The resulting images were processed using ImageJ. An oval ROI was placed on the tubes at each TE and TI for the determination of  $T_2$  and  $T_1$  relaxation times, respectively. Both  $r_1$  and  $r_2$  relaxivities were calculated through curve fitting of  $1/T_1$  or  $1/T_2$  ( $\text{ms}^{-1}$ ) as a function of AION (or iron) concentration (mM).

*NIRF optical imaging.* The phantom was constructed by placing different concentrations of AION (ranging from 0.02 to 0.5 mM of DiR) suspended in DI water into a black bottom 96 well plate ( $n = 3$ ). The plate was imaged using an IVIS Spectrum (PerkinElmer, Waltham, MA) with excitation and emission wavelengths at 710 nm and 780 nm, respectively. Finally, the images were processed using the Living Image 4.5.4 Software designed for IVIS imaging systems.

### ***In vivo imaging.***

*Animal experiments.* All in vivo experimental protocols were conducted in accordance with PHS policy on humane care and use of laboratory animals (Public Law 99-158) and with approval from the Institutional Animal Care and Use Committee of the University of Pennsylvania under protocol number 805593. Imaging experiments were performed using mice with breast tumors

( $n = 5$  per group). The breast cancer model was created by inoculating nude female mice (Taconic Biosciences, Hudson, NY) with MDA-MB-231 cells in their mammary glands ( $4 \times 10^6$  cells in 50  $\mu\text{L}$  HBSS). Tumors were grown to an approximate size of 100  $\text{mm}^3$  at 5 weeks post-inoculation and pre-contrast tumor images were acquired at this time. Immediately following the scans, a dose of 250 mg Ag/kg (or 25 mg Fe/kg) was administered *via* the tail vein. Mice were anesthetized with isoflurane during all imaging experiments.

*Dual energy mammography.* Tumor-bearing mice were imaged using the afore-mentioned Hologic Selenia Dimensions DEM prototype at several time points: pre-injection, 5, 30, 60, and 120 minutes. Images were acquired using the same conditions used for the DEM phantom imaging as described above *i.e.* HE (45 kV) and LE (26 kV) with a tungsten target. After DE subtraction, the DEM signals in the tumors and muscle near the hind leg were calculated using ImageJ by placing an oval ROI on the target in each image at each time point. The CNR (equation 2) in the tumors of each mouse was calculated and presented as mean  $\pm$  SEM.

$$CNR = \frac{|DEM\ contrast\ (tumor) - DEM\ contrast\ (muscle)|}{noise} \quad \text{Equation (2)}$$

*Computed tomography.* CT imaging experiments were performed using a MicroCAT II scanner (Imtek, Inc., Knoxville, TN) with the afore-mentioned tumor-bearing mice to investigate the CT contrast production from the AION. Mice were scanned prior to injection and at 2 and 24 hours post injection. CT images were acquired using the following parameters: slice thickness = 100  $\mu\text{m}$ , FOV = 51.2 x 76.8 mm, tube voltage = 80 kV, tube current = 500  $\mu\text{A}$ . A Feldkamp cone beam correction and a Shepp-Logan filter were used as the reconstruction kernel. The CT images were analyzed using Osirix 64-bit and the attenuation values in Hounsfield units (HU) for the tumors were measured from three different slices at each time point. Data are presented as mean  $\pm$  SEM.

*Magnetic resonance imaging.* MRI was performed using a 4.7 T 50 cm horizontal bore MR Spectrometer equipped with a 30 cm ID gauss/cm and a 12 cm ID gauss/cm gradient tube and interfaced to a Varian DirectDrive console.  $T_2^*$ -weighted MR images were acquired using a multi-gradient echo multi-slice sequence with a 35 mm coil under the following parameters: TR = 1000 ms, TI = 60 ms, NA = 3, FA = 90 degrees, number of echoes = 8, slice thickness = 1 mm, imaging matrix = 128 x 128 and FOV = 30 x 30 mm. TE values were chosen between 3.3 and 26.4 ms (with an interval of 3.3 ms). Post-contrast images of the tumor-bearing mice were acquired 24 hours after injection using the same imaging parameters as the pre-contrast images. Throughout the experiment, the respiratory rate of the mice was monitored and their body temperature was maintained at 37°C. Color coded  $R_2$  maps were generated from the MR images acquired with the above sequence using a custom written MATLAB program for pixel-wise curve fitting of the  $T_2$  relaxation times. The first four echo times from 3.3 ms to 13.2 ms were chosen to construct the maps. Mean  $R_2$  values were computed by averaging pixels within the tumor ROI for each mouse (three tumor slices per mouse). Squared correlation coefficient was also calculated to examine the quality of curve fitting for each pixel across the tumor regions. Results at each time point are presented as mean  $\pm$  SD.

*NIRF optical imaging.* Fluorescence imaging experiments were performed using an IVIS Spectrum system (PerkinElmer, Waltham, MA). Tumor-bearing mice were imaged before injection and 2 and 24 hours after injection using the DiR channel (745 nm excitation, 800 nm emission) with an exposure time of 1 second. All images had the same illumination settings and were analyzed using the Living Image 4.5.4 Software designed for IVIS imaging systems. The average radiant efficiency of each tumor image was recorded using the ROI tool. The tumor-to-background ratio was calculated at each time point and presented as mean  $\pm$  SEM.

**Biodistribution.** Tumor-bearing mice were sacrificed at 24 hours after injection and their blood samples were then collected. After the left ventricle was perfused with PBS, the liver, lungs, heart, spleen, kidneys, tumors and feces were collected. The organs and tumors were first weighed and minced into small pieces that were then digested in 2 ml of concentrated nitric acid at 75 °C for 16 hours. The digested samples were made to 10 ml with DI water for subsequent measurement of silver concentration *via* ICP-OES. Data are presented as mean  $\pm$  SEM.

**Pathology analysis.** Non tumor-bearing mice (n = 4 per group) were sacrificed at 24 hours after injection of PBS (vehicle control) or AION at a dose 250 mg Ag/kg (the same volume was used in each case). After the left ventricles were perfused with PBS, the livers and spleens were collected. The organs were briefly washed with cold PBS and cut into small pieces with thickness of 5 to 6 mm. The organ pieces were then fixed in 10% neutral buffered formalin and dehydrated with ethanol. Subsequently, tissues were embedded in paraffin, sectioned and stained with hematoxylin and eosin (H&E) for histological examination. The stained slices were analyzed with a light microscope (Nikon).

**Statistical analysis.** All experiments were carried out in triplicate at the least, or in three independent experiments. Statistical analyses were performed *via* two-tailed Student's *t*-tests using GraphPad Prism 6 software.

## Acknowledgements

This material is based upon work supported by the National Science Foundation Graduate Research Fellowship under Grant No. DGE-1321851 and the IGERT Complex Scene Perception program (J. Hsu). Partial support was provided by the NIH (R01s HL131557 and CA227142), a Breast Cancer Pilot Grant from the Abramson Cancer Center of the University of

Pennsylvania and a grant from the Pennsylvania Breast Cancer Coalition (all D. Cormode). The prototype DEM imaging system was provided to Penn by Hologic (Bedford, MA) under a research agreement.

**Supporting information available:** SEM of AION, EDX spectrum of AION, EDX line scan across a single AION particle, absorption and fluorescence emission spectra of AION, TEM of AgNP, CT attenuation of AION vs. concentration at various tube voltages, CT attenuation rate in units of HU mM<sup>-1</sup> for each tube voltage and representative H&E stained micrographs of mouse liver and spleen.

## References

1. Siu, A. L.; Force, U. S. P. S. T. Screening for Breast Cancer: U.S. Preventive Services Task Force Recommendation Statement. *Ann. Intern. Med.* **2016**, *164*, 279-296.
2. Wang, A. T.; Vachon, C. M.; Brandt, K. R.; Ghosh, K. Breast Density and Breast Cancer Risk: A Practical Review. *Mayo Clin. Proc.* **2014**, *89*, 548-557.
3. Carney, P. A.; Miglioretti, D. L.; Yankaskas, B. C.; Kerlikowske, K.; Rosenberg, R.; Rutter, C. M.; Geller, B. M.; Abraham, L. A.; Taplin, S. H.; Dignan, M., et al. Individual and Combined Effects of Age, Breast Density, and Hormone Replacement Therapy Use on the Accuracy of Screening Mammography. *Ann. Intern. Med.* **2003**, *138*, 168-175.
4. Mandelson, M. T.; Oestreicher, N.; Porter, P. L.; White, D.; Finder, C. A.; Taplin, S. H.; White, E. Breast Density as a Predictor of Mammographic Detection: Comparison of Interval- and Screen-Detected Cancers. *JNCI, J. Natl. Cancer Inst.* **2000**, *92*, 1081-1087.
5. McCormack, V. A.; dos Santos Silva, I. Breast Density and Parenchymal Patterns as Markers of Breast Cancer Risk: A Meta-Analysis. *Cancer Epidemiol., Biomarkers Prev.* **2006**, *15*, 1159-1169.
6. Perazella, M. A. Current Status of Gadolinium Toxicity in Patients with Kidney Disease. *Clin. J. Am. Soc. Nephrol.* **2009**, *4*, 461-469.
7. Rogosnitzky, M.; Branch, S. Gadolinium-Based Contrast Agent Toxicity: A Review of Known and Proposed Mechanisms. *BioMetals* **2016**, *29*, 365-376.
8. Kanda, T.; Fukusato, T.; Matsuda, M.; Toyoda, K.; Oba, H.; Kotoku, J.; Haruyama, T.; Kitajima, K.; Furui, S. Gadolinium-Based Contrast Agent Accumulates in the Brain Even in Subjects without Severe Renal Dysfunction: Evaluation of Autopsy Brain Specimens with Inductively Coupled Plasma Mass Spectroscopy. *Radiology* **2015**, *276*, 228-232.

9. McDonald, R. J.; McDonald, J. S.; Kallmes, D. F.; Jentoft, M. E.; Murray, D. L.; Thielen, K. R.; Williamson, E. E.; Eckel, L. J. Intracranial Gadolinium Deposition after Contrast-Enhanced MR Imaging. *Radiology* **2015**, *275*, 772-782.
10. Kanda, T.; Ishii, K.; Kawaguchi, H.; Kitajima, K.; Takenaka, D. High Signal Intensity in the Dentate Nucleus and Globus Pallidus on Unenhanced T1-Weighted MR Images: Relationship with Increasing Cumulative Dose of a Gadolinium-Based Contrast Material. *Radiology* **2014**, *270*, 834-841.
11. Errante, Y.; Cirimele, V.; Mallio, C. A.; Di Lazzaro, V.; Zobel, B. B.; Quattrocchi, C. C. Progressive Increase of T1 Signal Intensity of the Dentate Nucleus on Unenhanced Magnetic Resonance Images is Associated with Cumulative Doses of Intravenously Administered Gadodiamide in Patients with Normal Renal Function, Suggesting Dechelation. *Invest. Radiol.* **2014**, *49*, 685-690.
12. Hosoya, T.; Yamaguchi, K.; Akutsu, T.; Mitsuhashi, Y.; Kondo, S.; Sugai, Y.; Adachi, M. Delayed Adverse Reactions to Iodinated Contrast Media and Their Risk Factors. *Radiat. Med.* **2000**, *18*, 39-45.
13. Namasivayam, S.; Kalra, M. K.; Torres, W. E.; Small, W. C. Adverse Reactions to Intravenous Iodinated Contrast Media: A Primer for Radiologists. *Emerg. Radiol.* **2006**, *12*, 210-215.
14. Tepel, M.; Aspelin, P.; Lameire, N. Contrast-Induced Nephropathy: A Clinical and Evidence-Based Approach. *Circulation* **2006**, *113*, 1799-1806.
15. Karunamuni, R.; Tsourkas, A.; Maidment, A. D. Exploring Silver as a Contrast Agent for Contrast-Enhanced Dual-Energy X-Ray Breast Imaging. *Br. J. Radiol.* **2014**, *87*, 20140081.
16. Artemov, D.; Mori, N.; Okollie, B.; Bhujwala, Z. M. MR Molecular Imaging of the HER-2/Neu Receptor in Breast Cancer Cells Using Targeted Iron Oxide Nanoparticles. *Magn. Reson. Med.* **2003**, *49*, 403-408.

17. Balasundaram, G.; Ho, C. J.; Li, K.; Driessen, W.; Dinish, U. S.; Wong, C. L.; Ntziachristos, V.; Liu, B.; Olivo, M. Molecular Photoacoustic Imaging of Breast Cancer Using an Actively Targeted Conjugated Polymer. *Int. J. Nanomed.* **2015**, *10*, 387-397.
18. Kinsella, J. M.; Jimenez, R. E.; Karmali, P. P.; Rush, A. M.; Kotamraju, V. R.; Gianneschi, N. C.; Ruoslahti, E.; Stupack, D.; Sailor, M. J. X-Ray Computed Tomography Imaging of Breast Cancer by Using Targeted Peptide-Labeled Bismuth Sulfide Nanoparticles. *Angew. Chem., Int. Ed. Engl.* **2011**, *50*, 12308-12311.
19. Zhang, Y.; Zhang, B.; Liu, F.; Luo, J.; Bai, J. In Vivo Tomographic Imaging with Fluorescence and MRI Using Tumor-Targeted Dual-Labeled Nanoparticles. *Int. J. Nanomed.* **2014**, *9*, 33-41.
20. Naha, P. C.; Lau, K. C.; Hsu, J. C.; Hajfathalian, M.; Mian, S.; Chhour, P.; Uppuluri, L.; McDonald, E. S.; Maidment, A. D.; Cormode, D. P. Gold Silver Alloy Nanoparticles (GSAN): An Imaging Probe for Breast Cancer Screening with Dual-Energy Mammography or Computed Tomography. *Nanoscale* **2016**, *8*, 13740-13754.
21. Karunamuni, R.; Naha, P. C.; Lau, K. C.; Al-Zaki, A.; Popov, A. V.; Delikatny, E. J.; Tsourkas, A.; Cormode, D. P.; Maidment, A. D. Development of Silica-Encapsulated Silver Nanoparticles as Contrast Agents Intended for Dual-Energy Mammography. *Eur. J. Radiol.* **2016**, *26*, 3301-3309.
22. Wang, Y. X. Superparamagnetic Iron Oxide Based MRI Contrast Agents: Current Status of Clinical Application. *Quant. Imaging Med. Surg.* **2011**, *1*, 35-40.
23. Levard, C.; Hotze, E. M.; Colman, B. P.; Dale, A. L.; Truong, L.; Yang, X. Y.; Bone, A. J.; Brown, G. E.; Tanguay, R. L.; Di Giulio, R. T., et al. Sulfidation of Silver Nanoparticles: Natural Antidote to Their Toxicity. *Environ. Sci. Technol.* **2013**, *47*, 13440-13448.
24. Mineral Commodity Summaries 2017 - Sulfur. <https://minerals.usgs.gov/minerals/pubs/commodity/sulfur/mcs-2017-sulfu.pdf> (accessed November 1, 2017).

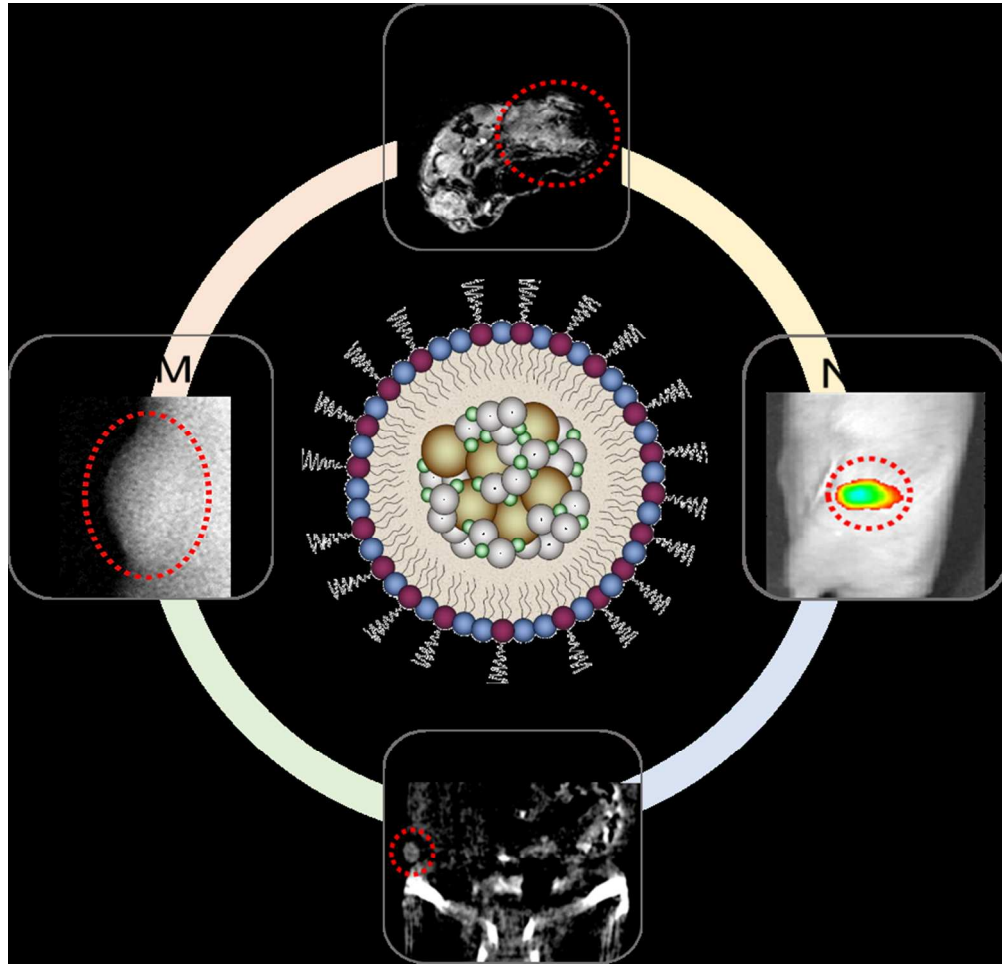
25. Zhang, Y.; Zhang, Y.; Hong, G.; He, W.; Zhou, K.; Yang, K.; Li, F.; Chen, G.; Liu, Z.; Dai, H., et al. Biodistribution, Pharmacokinetics and Toxicology of Ag<sub>2</sub>S Near-Infrared Quantum Dots in Mice. *Biomaterials* **2013**, *34*, 3639-3646.
26. Li, C.; Zhang, Y.; Wang, M.; Zhang, Y.; Chen, G.; Li, L.; Wu, D.; Wang, Q. In Vivo Real-Time Visualization of Tissue Blood Flow and Angiogenesis Using Ag<sub>2</sub>S Quantum Dots in the NIR-II Window. *Biomaterials* **2014**, *35*, 393-400.
27. Kastantin, M.; Ananthanarayanan, B.; Karmali, P.; Ruoslahti, E.; Tirrell, M. Effect of the Lipid Chain Melting Transition on the Stability of DSPE-PEG(2000) Micelles. *Langmuir* **2009**, *25*, 7279-7286.
28. Torchilin, V. P. PEG-Based Micelles as Carriers of Contrast Agents for Different Imaging Modalities. *Adv. Drug Delivery Rev.* **2002**, *54*, 235-252.
29. Jarzyna, P. A.; Skajaa, T.; Gianella, A.; Cormode, D. P.; Samber, D. D.; Dickson, S. D.; Chen, W.; Griffioen, A. W.; Fayad, Z. A.; Mulder, W. J. Iron Oxide Core Oil-In-Water Emulsions as a Multifunctional Nanoparticle Platform for Tumor Targeting and Imaging. *Biomaterials* **2009**, *30*, 6947-6954.
30. Kumar, R.; Ohulchansky, T. Y.; Roy, I.; Gupta, S. K.; Borek, C.; Thompson, M. E.; Prasad, P. N. Near-Infrared Phosphorescent Polymeric Nanomicelles: Efficient Optical Probes for Tumor Imaging and Detection. *ACS Appl. Mater. Interfaces* **2009**, *1*, 1474-1481.
31. Farrell, Z.; Shelton, C.; Dunn, C.; Green, D. Straightforward, One-Step Synthesis of Alkanethiol-Capped Silver Nanoparticles from an Aggregative Model of Growth. *Langmuir* **2013**, *29*, 9291-9300.
32. Liu, J.; Hurt, R. H. Ion Release Kinetics and Particle Persistence in Aqueous Nano-Silver Colloids. *Environ. Sci. Technol.* **2010**, *44*, 2169-2175.
33. Greulich, C.; Diendorf, J.; Simon, T.; Eggeler, G.; Epple, M.; Koller, M. Uptake and Intracellular Distribution of Silver Nanoparticles in Human Mesenchymal Stem Cells. *Acta Biomater.* **2011**, *7*, 347-354.

34. Loza, K.; Diendorf, J.; Sengstock, C.; Ruiz-Gonzalez, L.; Gonzalez-Calbet, J. M.; Vallet-Regi, M.; Koller, M.; Epple, M. The Dissolution and Biological Effects of Silver Nanoparticles in Biological Media. *J. Mater. Chem. B* **2014**, *2*, 1634-1643.
35. Levard, C.; Reinsch, B. C.; Michel, F. M.; Oumahi, C.; Lowry, G. V.; Brown, G. E. Sulfidation Processes of PVP-Coated Silver Nanoparticles in Aqueous Solution: Impact on Dissolution Rate. *Environ. Sci. Technol.* **2011**, *45*, 5260-5266.
36. Levard, C.; Hotze, E. M.; Lowry, G. V.; Brown, G. E., Jr. Environmental Transformations of Silver Nanoparticles: Impact on Stability and Toxicity. *Environ. Sci. Technol.* **2012**, *46*, 6900-6914.
37. Carton, A. K.; Gavenonis, S. C.; Currivan, J. A.; Conant, E. F.; Schnall, M. D.; Maidment, A. D. Dual-Energy Contrast-Enhanced Digital Breast Tomosynthesis--A Feasibility Study. *Br. J. Radiol.* **2010**, *83*, 344-350.
38. Carton, A. K.; Ullberg, C.; Lindman, K.; Acciavatti, R.; Francke, T.; Maidment, A. D. Optimization of a Dual-Energy Contrast-Enhanced Technique for a Photon-Counting Digital Breast Tomosynthesis System: I. A Theoretical Model. *Med. Phys.* **2010**, *37*, 5896-5907.
39. Zhang, X.; Yao, M.; Chen, M.; Li, L.; Dong, C.; Hou, Y.; Zhao, H.; Jia, B.; Wang, F. Hyaluronic Acid-Coated Silver Nanoparticles as a Nanoplatfor for In Vivo Imaging Applications. *ACS Appl. Mater. Interfaces* **2016**, *8*, 25650-25653.
40. Galper, M. W.; Saung, M. T.; Fuster, V.; Roessl, E.; Thran, A.; Proksa, R.; Fayad, Z. A.; Cormode, D. P. Effect of Computed Tomography Scanning Parameters on Gold Nanoparticle and Iodine Contrast. *Invest. Radiol.* **2012**, *47*, 475-481.
41. Lindfors, K. K.; Boone, J. M.; Nelson, T. R.; Yang, K.; Kwan, A. L.; Miller, D. F. Dedicated Breast CT: Initial Clinical Experience. *Radiology* **2008**, *246*, 725-733.
42. Prionas, N. D.; Lindfors, K. K.; Ray, S.; Huang, S. Y.; Beckett, L. A.; Monsky, W. L.; Boone, J. M. Contrast-Enhanced Dedicated Breast CT: Initial Clinical Experience. *Radiology* **2010**, *256*, 714-723.

43. Qin, M. Y.; Yang, X. Q.; Wang, K.; Zhang, X. S.; Song, J. T.; Yao, M. H.; Yan, D. M.; Liu, B.; Zhao, Y. D. In Vivo Cancer Targeting and Fluorescence-CT Dual-Mode Imaging with Nanoprobes Based on Silver Sulfide Quantum Dots and Iodinated Oil. *Nanoscale* **2015**, *7*, 19484-19492.
44. Zhang, J.; Li, C.; Zhang, X.; Huo, S.; Jin, S.; An, F. F.; Wang, X.; Xue, X.; Okeke, C. I.; Duan, G., et al. In Vivo Tumor-Targeted Dual-Modal Fluorescence/CT Imaging Using a Nanoprobe Co-Loaded with an Aggregation-Induced Emission Dye and Gold Nanoparticles. *Biomaterials* **2015**, *42*, 103-111.
45. Cormode, D. P.; Skajaa, G. O.; Delshad, A.; Parker, N.; Jarzyna, P. A.; Calcagno, C.; Galper, M. W.; Skajaa, T.; Briley-Saebo, K. C.; Bell, H. M., et al. A Versatile and Tunable Coating Strategy Allows Control of Nanocrystal Delivery to Cell Types in the Liver. *Bioconjugate Chem.* **2011**, *22*, 353-361.
46. Klibanov, A. L.; Maruyama, K.; Beckerleg, A. M.; Torchilin, V. P.; Huang, L. Activity of Amphipathic Poly(Ethylene Glycol) 5000 to Prolong the Circulation Time of Liposomes Depends on the Liposome Size and is Unfavorable for Immunoliposome Binding to Target. *Biochim. Biophys. Acta* **1991**, *1062*, 142-148.
47. Cheung, Y. C.; Lin, Y. C.; Wan, Y. L.; Yeow, K. M.; Huang, P. C.; Lo, Y. F.; Tsai, H. P.; Ueng, S. H.; Chang, C. J. Diagnostic Performance of Dual-Energy Contrast-Enhanced Subtracted Mammography in Dense Breasts Compared to Mammography Alone: Interobserver Blind-Reading Analysis. *Eur. J. Radiol.* **2014**, *24*, 2394-2403.
48. Jochelson, M. S.; Dershaw, D. D.; Sung, J. S.; Heerdt, A. S.; Thornton, C.; Moskowitz, C. S.; Ferrara, J.; Morris, E. A. Bilateral Contrast-Enhanced Dual-Energy Digital Mammography: Feasibility and Comparison with Conventional Digital Mammography and MR Imaging in Women with Known Breast Carcinoma. *Radiology* **2013**, *266*, 743-751.

49. Luczynska, E.; Heinze-Paluchowska, S.; Hendrick, E.; Dyczek, S.; Rys, J.; Herman, K.; Blecharz, P.; Jakubowicz, J. Comparison Between Breast MRI and Contrast-Enhanced Spectral Mammography. *Med. Sci. Monit.* **2015**, *21*, 1358-1367.
50. Berg, W. A.; Zhang, Z.; Lehrer, D.; Jong, R. A.; Pisano, E. D.; Barr, R. G.; Bohm-Velez, M.; Mahoney, M. C.; Evans, W. P., 3rd; Larsen, L. H., et al. Detection of Breast Cancer with Addition of Annual Screening Ultrasound or a Single Screening MRI to Mammography in Women with Elevated Breast Cancer Risk. *JAMA* **2012**, *307*, 1394-1404.
51. Dewey, M.; Schink, T.; Dewey, C. F. Claustrophobia During Magnetic Resonance Imaging: Cohort Study in Over 55,000 Patients. *J. Magn. Reson. Imaging* **2007**, *26*, 1322-1327.
52. Enders, J.; Zimmermann, E.; Rief, M.; Martus, P.; Klingebiel, R.; Asbach, P.; Klessen, C.; Diederichs, G.; Bengner, T.; Teichgraber, U., et al. Reduction of Claustrophobia During Magnetic Resonance Imaging: Methods and Design of the "Claustro" Randomized Controlled Trial. *BMC Med. Imaging* **2011**, *11*, 4.
53. Louie, A. Multimodality Imaging Probes: Design and Challenges. *Chem. Rev.* **2010**, *110*, 3146-3195.
54. Ni, D.; Bu, W.; Ehlerding, E. B.; Cai, W.; Shi, J. Engineering of Inorganic Nanoparticles as Magnetic Resonance Imaging Contrast Agents. *Chem. Soc. Rev.* **2017**, *46*, 7438-7468.
55. Gold price. <http://goldprice.org> (accessed February 16, 2018).
56. Silver price. <http://silverprice.org> (accessed February 16, 2018).
57. Zhang, Y.; Hong, G.; Zhang, Y.; Chen, G.; Li, F.; Dai, H.; Wang, Q. Ag<sub>2</sub>S Quantum Dot: A Bright and Biocompatible Fluorescent Nanoprobe in the Second Near-Infrared Window. *ACS Nano* **2012**, *6*, 3695-3702.
58. Cheheltani, R.; Ezzibdeh, R. M.; Chhour, P.; Pulaparthy, K.; Kim, J.; Jurcova, M.; Hsu, J. C.; Blundell, C.; Litt, H. I.; Ferrari, V. A., et al. Tunable, Biodegradable Gold Nanoparticles as Contrast Agents for Computed Tomography and Photoacoustic Imaging. *Biomaterials* **2016**, *102*, 87-97.

59. Erhard, K.; Kilburn-Toppin, F.; Willsher, P.; Moa, E.; Fredenberg, E.; Wieberneit, N.; Buelow, T.; Wallis, M. G. Characterization of Cystic Lesions by Spectral Mammography: Results of a Clinical Pilot Study. *Invest. Radiol.* **2016**, *51*, 340-347.
60. Fredenberg, E.; Kilburn-Toppin, F.; Willsher, P.; Moa, E.; Danielsson, M.; Dance, D. R.; Young, K. C.; Wallis, M. G. Measurement of Breast-Tissue X-Ray Attenuation by Spectral Mammography: Solid Lesions. *Phys. Med. Biol.* **2016**, *61*, 2595-2612.



161x155mm (150 x 150 DPI)